



Selective catalytic reduction of NO with NH₃ over HZSM-5-supported Fe–Cu nanocomposite catalysts: The Fe–Cu bimetallic effect

Tao Zhang, Jian Liu*, Daxi Wang, Zhen Zhao*, Yuechang Wei, Kai Cheng, Guiyuan Jiang, Aijun Duan

State Key Laboratory of Heavy Oil Processing, China University of Petroleum, Beijing 102249, China

ARTICLE INFO

Article history:

Received 16 July 2013

Received in revised form

26 September 2013

Accepted 6 November 2013

Available online 15 November 2013

Keywords:

Selective catalytic reduction

Iron

Fe–Cu nanocomposites

Fe_x–Cu₄/ZSM-5

Catalytic activity

ABSTRACT

A series of Fe_x–Cu₄/ZSM-5 catalysts with fixed Cu content and variable Fe loading amounts were synthesized by an improved incipient-wetness-impregnation method, and their catalytic performances were tested for selective catalytic reduction (SCR) of NO with ammonia as reductant. The catalysts were characterized by means of XRD, BET, SEM, TEM, FT-IR, UV–vis DRS, UV-Raman, NH₃-TPD, Py-IR, H₂-TPR and XPS. The results indicated that the high activities of Fe_x–Cu₄/ZSM-5 could be attributed to the formation of Fe–Cu nanocomposites with high dispersion. The interaction between the iron and copper species in the Fe–Cu nanocomposites leads to the change of electronic properties, the stronger redox ability and more acid sites over catalyst surface for Fe_x–Cu₄/ZSM-5 comparing with Cu₄/ZSM-5. Thus, the addition of iron to Cu₄/ZSM-5 catalyst improved its catalytic performance, and Fe₄–Cu₄/ZSM-5 catalyst exhibited the high NO conversion (>90%) among the wide temperature range (200–475 °C).

© 2013 Elsevier B.V. All rights reserved.

1. Introduction

Nitrogen oxides, such as NO, NO₂, and N₂O₅ (NO_x), which originate from various combustion processes, are a major kind of air pollutants and are very harmful to human health due to the formation of photochemical smog, acid rain, ozone depletion and greenhouse effects. NO_x emissions from a typical refinery are about 2000 tons/year, and the fluid catalytic cracking (FCC) section contributes about 50% of this amount [1]. Regulations that confine the emissions of NO_x from the regenerator of a FCC unit are becoming more and more stringent due to environmental concerns and to the use of heavier feedstocks [2].

The selective catalytic reduction (SCR) of NO_x with ammonia is a very effective technology for eliminating NO_x in the flue gas from stationary sources and motor vehicles [3,4]. The V-based catalyst is usually used for NH₃-SCR of NO_x and V₂O₅–WO₃(MoO₃)/TiO₂ as a commercial catalyst exhibits high catalytic activity and selectivity [5]. However, there are still some inevitable problems, such as the high working temperature, the toxicity of vanadium species [6,7], high activity for oxidation of SO₂ to SO₃ [8], and the low N₂ selectivity in the high temperature range [9,10]. Therefore, it is important to

develop vanadium-free SCR catalysts with relatively low working temperature [11].

In the recent years, zeolite-based materials have attracted much attention, and there has been a significant interest in developing zeolite-based catalysts for NH₃-SCR [12,13]. Zeolites indeed offer a number of advantages over V–Ti catalysts. They are active and selective over a wider temperature range, and are more thermally stable. Moreover, zeolite-based catalysts exhibit very low selectivity to N₂O, with regard to N₂, even at high temperature. Zeolite-based catalysts promoted by transition metals are being considered for practical applications in FCC regeneration flue gas due to their high NO_x removal efficiency over a wide temperature range. Among zeolite-based catalysts, Cu–ZSM-5 and Fe–ZSM-5 catalysts show good catalytic performance for the SCR of NO_x by NH₃ [14,15]. Meanwhile, Cu/ZSM-5 catalyst exhibits the low-temperature activity (<350 °C), and Fe/ZSM-5 catalyst mainly contributes to the high-temperature activity (>350 °C).

There is still a debate in the literature about the identity and nuclearity of active sites for SCR chemistry on transition metals supported on zeolites. Kieger et al. [16] proposed that for NH₃-SCR over Cu-FAU at temperatures below 300 °C, the active sites be formed by neighboring Cu ions, which may be [CuOCu]²⁺ dimer species. Above 350 °C, however, all Cu ions become active. In contrast to copper zeolites, several active sites for iron zeolites, such as small Fe_xO_y clusters or oxygen bridged binuclear iron species like [HO–Fe–O–Fe–OH]²⁺ [17], isolated Fe²⁺ and Fe³⁺ ions [18], have been postulated.

* Corresponding authors at: 18# Fuxue Road, Chang Ping District, Beijing 102249, China. Tel.: +86 10 89731586; fax: +86 10 69724721.

E-mail addresses: liujian@cup.edu.cn (J. Liu), zhenzhao@cup.edu.cn (Z. Zhao).

At present, most of reports are focused on incorporation of single metal ions. To the best of our knowledge, little attention has paid to texture, structure, redox property, surface state and activity of NO reduction by NH_3 over the Fe–Cu bimetallic-based ZSM-5 catalyst. The bimetallic-based catalysts usually show complementary advantages and synergistic effects. The performances of these bimetallic catalysts are influenced by metal–metal bonds [19]. Herein, we attempt to modify the $\text{Cu}_4/\text{ZSM-5}$ catalyst with iron to develop a more efficient catalyst for NH_3 -SCR. The study is mainly focused on: (i) the influence of iron introduction on the structure of the catalysts and the chemical state of copper and iron species; (ii) to gain insights into the probable active and acid sites for the NH_3 -SCR reaction over the Fe–Cu bimetallic catalysts.

2. Experimental

2.1. Preparation of $\text{Fe}_x\text{-Cu}_4/\text{ZSM-5}$ catalysts

A series of $\text{Fe}_x\text{-Cu}_4/\text{ZSM-5}$ catalysts with fixed copper content of 4 wt% and variable iron loading amounts were prepared by an improved incipient-wetness-impregnation method. To achieve incipient wetness a liquid/solid ratio of 0.60 mL/g was used. In a typical synthesis, the support of 5 g HZSM-5 was preheated in a vacuum oven at 100°C to remove the adsorbed water. Then the required amount of an aqueous solution of $\text{Cu}(\text{NO}_3)_2$ and $\text{Fe}(\text{NO}_3)_3$ was slowly added to the support with thoroughly stirring at room temperature, and then ultrasonic treatment for 1 h. Copper loading amount for all catalysts was maintained at 4 wt%, with iron content at 2, 4, 6 and 8 wt%, respectively. The precursor was dried at 100°C for 12 h, and consequently calcined in air at 550°C for 6 h. The final catalyst was labeled as $\text{Fe}_x\text{-Cu}_4/\text{ZSM-5}$ (x denotes the weight percentage of Fe to support ZSM-5, $x = 2, 4, 6, 8$).

To determine the optimum copper loading amount and compare the catalytic activity for NH_3 -SCR over different types of catalysts, the $\text{Cu}_y/\text{ZSM-5}$ catalysts with different copper loading amounts (y denotes the weight percentage of Cu to support ZSM-5, $y = 2, 4, 6, 8$) were prepared by the above method.

2.2. Physical and chemical characterization

N_2 adsorption–desorption isotherm was measured at 77 K using a Micromeritics TriStar II 2020 porosimetry analyzer. The samples were degassed at 300°C for 8 h prior to the measurements. The specific surface area was calculated according to the Brunauer–Emmett–Teller (BET) method. The total pore volume depended on the absorbed N_2 volume at a relative pressure of approximately 0.99.

Powder XRD patterns were obtained by a powder X-ray diffractometer (Shimadzu XRD 6000) using $\text{Cu K}\alpha$ ($\lambda = 0.15406\text{ nm}$) radiation with a Nickel filter operating at 40 kV and 10 mA in the 2θ range of $5\text{--}70^\circ$ at a scanning rate of $4^\circ/\text{min}$. The diffraction lines were identified by matching them with reference patterns in the JCPDS database.

The surface morphology of the catalyst was observed by field emission scanning electron microscopy (FESEM) on a Quanta 200F instruments using accelerating voltages of 5 kV, in combination with an EDAX genesis 4000 energy-dispersive X-ray spectrometer (EDX). Samples for SEM were dusted on an adhesive conductive carbon belt attached to a copper disk and were coated with 10 nm Au prior to measurement.

The TEM images were carried out using a JEOL JEM 2100 electron microscope equipped with a field emission source at an accelerating voltage of 200 kV. The average particle diameter was calculated

from the mean diameter frequency distribution with the formula: $d = \sum n_i d_i / \sum n_i$, where n_i is the number of particles with particle diameter d_i in a certain range. The elemental local, mapping and line-scanning analyses were acquired by energy-dispersive spectroscopy (EDS) using a Tecnai F20 electron microscope equipped with a STEM unit and a CCD detector.

Fourier transform infrared (FT-IR) absorbance spectra were recorded in the wave numbers ranging from 4000 to 400 cm^{-1} via a FTS-3000 spectrophotometer. The measured wafer was prepared with the weight ratio of sample to KBr, 1/100. The resolution was set at 2 cm^{-1} during measurements.

The UV–vis diffuse reflectance spectroscopy (UV–vis DRS) experiments were performed on a UV–vis spectrophotometer (Hitachi U-4100) with the integration sphere diffuse reflectance attachment.

UV-Raman spectra were recorded with a Renishaw Micro-Raman System 2000 spectrometer with spectral resolution of 2 cm^{-1} . The laser line at 325 nm of a He/Cd laser was used as exciting source with an output of 20 mW.

X-ray photoelectron spectra (XPS) were recorded on a PerkinElmer PHI-1600 ESCA spectrometer using $\text{Mg K}\alpha$ ($h\nu = 1253.6\text{ eV}$, $1\text{ eV} = 1.603 \times 10^{-19}\text{ J}$) X-ray source. The binding energies were calibrated using C1s peak of contaminant carbon ($\text{BE} = 284.6\text{ eV}$) as an internal standard.

Temperature-programmed desorption of ammonia (NH_3 -TPD) was performed in a conventional flow apparatus. Before TPD, each sample was pretreated with high-purity (99.999%) N_2 (40 mL/min) at 500°C for 1 h, then saturated with high-purity anhydrous ammonia at 100°C for 1 h and subsequently flushed at the same temperature for 1 h to remove physisorbed ammonium. Finally, the TPD operation was carried out from 100 to 700°C at a heating rate of $10^\circ\text{C}/\text{min}$. The amount of NH_3 desorbed was monitored by a thermal conductivity detector (TCD).

The nature of the acid sites of the catalysts was determined by pyridine-IR on a MAGNAIR 560 FT-IR instrument with a resolution of 1 cm^{-1} . The samples were dehydrated at 500°C for 5 h under a vacuum of $1.33 \times 10^{-3}\text{ Pa}$, followed by adsorption of purified pyridine vapor at room temperature for 20 min. The system was then degassed and evacuated at different temperatures, and the Py-IR spectra were recorded.

Temperature-programmed reduction with H_2 (H_2 -TPR) measurements were performed in a conventional flow apparatus. 100 mg sample was pretreated under air atmosphere by calcination at 300°C for 1 h and subsequently cooled to 30°C . Afterwards, 10% H_2/Ar flow (40 mL/min) was passed over the catalyst bed while the temperature was ramped from 30 to 600°C at a heating rate of $10^\circ\text{C}/\text{min}$. The hydrogen consumption signal was monitored by a TCD. Before the outlet gases entering the TCD, a cooling trap and a filter packed with molecular sieve 5A (60–80 meshes) were used to remove H_2O and CO_2 .

2.3. Activity measurements

The NH_3 -SCR activity measurements were carried out in a fixed bed quartz micro-reactor operating in a steady flow mode. 0.4 g of catalysts were sieved with 40–60 mesh and used in each test. The reactant gas composition was typically: 1000 ppm NO, 1000 ppm NH_3 , 3% O_2 and balance N_2 . The total flow rate was 500 mL/min and thus a GHSV of $45,000\text{ h}^{-1}$ was obtained. The temperature varied from 100 to 500°C . The data was recorded when the SCR reaction reached steady state after 10 min at each measuring temperature. The concentration of NO_x ($\text{NO}_x = \text{NO} + \text{NO}_2$) in the inlet and outlet gas mixture was measured by a SIGNAL 4000 VM NO_x analyzer. Meanwhile, the concentration of NH_3 , NO, NO_2 and N_2O were measured by a FTIR spectrometer (MKS, MultiGas 2030HS).

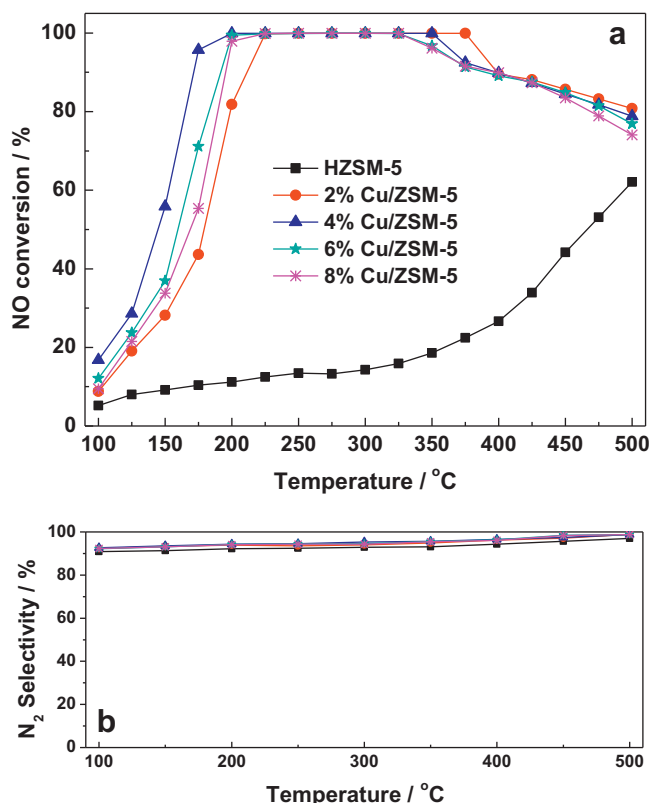


Fig. 1. NO conversion (a) and N_2 selectivity (b) as a function of reaction temperature over HZSM-5 and $Cu_4/ZSM-5$ catalysts with different copper loadings.

The NO conversion was calculated based on the inlet and outlet gas concentrations at steady state, as shown in Eq. (1).

$$\text{NO conversion (\%)} = \frac{[NO]_{\text{inlet}} - [NO]_{\text{outlet}}}{[NO]_{\text{inlet}}} \times 100 \quad (1)$$

The N_2 selectivity in SCR reaction was calculated from Eq. (2) [20].

$$N_2 \text{ selectivity (\%)} = \left(1 - \frac{2[N_2O]_{\text{outlet}}}{[NO_x]_{\text{inlet}} + [NH_3]_{\text{inlet}} - [NO_x]_{\text{outlet}} - [NH_3]_{\text{outlet}}} \right) \times 100 \quad (2)$$

3. Results

3.1. NH_3 -SCR catalytic activity

$Cu_4/ZSM-5$ catalysts are tested in the NH_3 -SCR of NO and the results are shown in Fig. 1a. The activity of pure HZSM-5 is also investigated for comparison. In these experiments, the NO conversion changes with the increasing of reaction temperature over all the samples. For pure HZSM-5, the maximum NO conversion is only 62.1% in the whole temperature range. The NO conversion increases when copper is introduced to the HZSM-5 support. The $Cu_4/ZSM-5$ catalyst shows the best catalytic performance with NO conversion above 90% from 175 to 375 °C. The temperature window of $Cu_2/ZSM-5$ shifts towards the high temperature range to a certain extent compared with $Cu_4/ZSM-5$. For $Cu_6/ZSM-5$ and $Cu_8/ZSM-5$, the activity temperature windows are much narrower than that of $Cu_4/ZSM-5$. In addition, as presented in Fig. 1b, N_2 selectivity was above 90% over all catalysts. Based on the above results, we chose copper loading amount of 4 wt% as the candidate for the next preparation of $Fe_x-Cu_4/ZSM-5$.

Fig. 2a shows the results of NO conversion in NH_3 -SCR reactions over $Cu_4/ZSM-5$ and $Fe_x-Cu_4/ZSM-5$ catalysts in the temperature

range of 100–500 °C. For more clearly exhibiting the catalytic performances in the low and high temperature range, Fig. 2b and c displays the NO conversion in 100–200 °C and 375–500 °C, respectively. When appropriate amounts of iron are added to $Cu_4/ZSM-5$, a significant influence on catalytic activity is observed. The temperature range for optimum NO reduction (>99%) extends toward higher temperature, corresponding to active window broadening. Among all the catalysts tested in this study, $Fe_4-Cu_4/ZSM-5$ catalyst exhibits the widest temperature window of catalytic activity for the removal of NO. The highest temperature to maintain NO conversion of 90% is 475 °C. For $Cu_4/ZSM-5$ catalyst, it keeps at 375 °C. For $Fe_4-Cu_4/ZSM-5$ catalyst, the temperature range is between 200 °C and 475 °C for NO removal above 90%. However, to achieve the same level of NO conversion for $Cu_4/ZSM-5$ and $Fe_2-Cu_4/ZSM-5$ catalysts, temperature range of 175–375 °C and 250–425 °C are required, respectively. Meanwhile, the large amounts of iron addition (6 wt%, 8 wt%) lead to a decreasing activity, which may be due to the occurrence of unselective oxidation of NH_3 [21]. The catalytic behaviors of $Fe_x-Cu_4/ZSM-5$ catalysts are very similar in the temperature range between 200 and 375 °C, and catalytic activity could not be linked to the different amount of Fe in the catalyst for this temperature range. However, in the low temperature range (100–200 °C, see Fig. 2b) and the high temperature range (375–500 °C, see Fig. 2c), the catalytic behaviors of $Fe_x-Cu_4/ZSM-5$ catalysts are associated with the amount of Fe addition, and $Fe_4-Cu_4/ZSM-5$ gave the highest catalytic activity among $Fe_x-Cu_4/ZSM-5$ catalysts. Furthermore, it should be noted that the NO conversion decreased at 350 °C or higher temperature, but it does not mean the deterioration of the present catalysts. Each catalyst has an operation temperature window, the NO conversion decreases significantly with the increase of reaction temperature due to the increased rate of unselective oxidation of NH_3 . Some similar phenomena were also reported in the literature [22,23]. Moreover, the N_2 selectivity of $Fe_x-Cu_4/ZSM-5$ and $Cu_4/ZSM-5$ catalysts (see Fig. 2d), which are similar each other in the whole temperature range, was above 90%.

The results of activity test suggest that a synergistic effect may be originated from the incorporation of iron in close proximity to copper. The experimental results in the following characterization sections will supply more information about the structure-activity relationship of these Fe–Cu based catalysts in the NH_3 -SCR reaction.

3.2. Catalyst characterization

3.2.1. The results of XRD

Fig. 3 shows the XRD patterns of pure HZSM-5, $Cu_4/ZSM-5$ and $Fe_x-Cu_4/ZSM-5$ catalysts with fixed Cu content and variable Fe loading amount. All the samples exhibit the typical peaks of ZSM-5 zeolite, indicating that the original zeolite structure remains intact. The intensity of the ZSM-5 principal diffraction peaks decreases with copper addition and the increasing of iron content, due to the higher absorption coefficient of copper and iron compounds for the X-ray radiation [24]. The phases of CuO (PDF# 48-1548) are not detected among $Cu_4/ZSM-5$ and $Fe_x-Cu_4/ZSM-5$ samples. When the loading amount of Fe is less than 4 wt%, no peaks for $\alpha-Fe_2O_3$ species (PDF# 33-0664) are observed in $Fe_x-Cu_4/ZSM-5$ samples. These results show that the copper and iron species are finely dispersed on the surface of ZSM-5 support as amorphous oxides, or that the copper and iron species consist of copper and iron oxides particles in the form of nanocomposites, which may be helpful to enhance NH_3 -SCR activity. Moreover, for $Fe_6-Cu_4/ZSM-5$ and $Fe_8-Cu_4/ZSM-5$ samples, low intensities of diffraction peaks at $2\theta = 33.2^\circ$, 35.6° , 40.9° , 49.5° , 54.1° and 62.4° can be observed, which is attributed to crystallite $\alpha-Fe_2O_3$ existing on the zeolite support. Based on the catalytic activity results, we can deduce that the crystalline $\alpha-Fe_2O_3$ do not contribute to the activity of NH_3 -SCR.

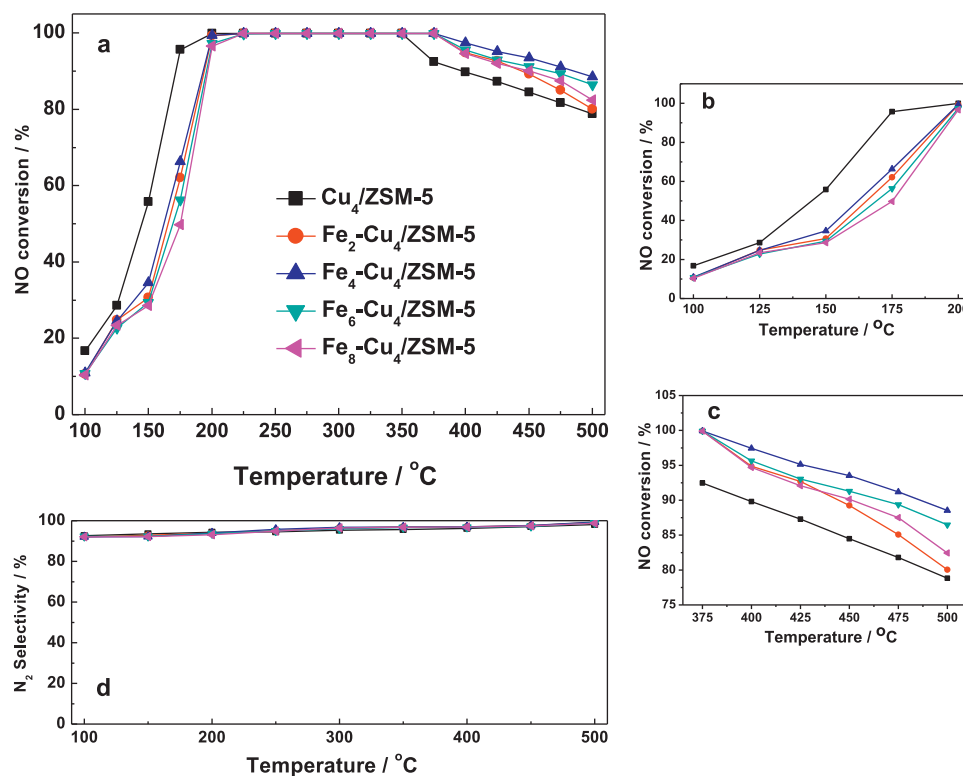


Fig. 2. NO conversion (a) and N₂ selectivity (b) as a function of reaction temperature over Cu₄/ZSM-5 and Fe_x-Cu₄/ZSM-5 catalysts with fixed Cu loadings and variable Fe loadings in the temperatures ranges of 100–500 °C (a); 100–200 °C (b); 375–500 °C (c); and N₂ selectivity in the temperatures ranges of 100–500 °C (d).

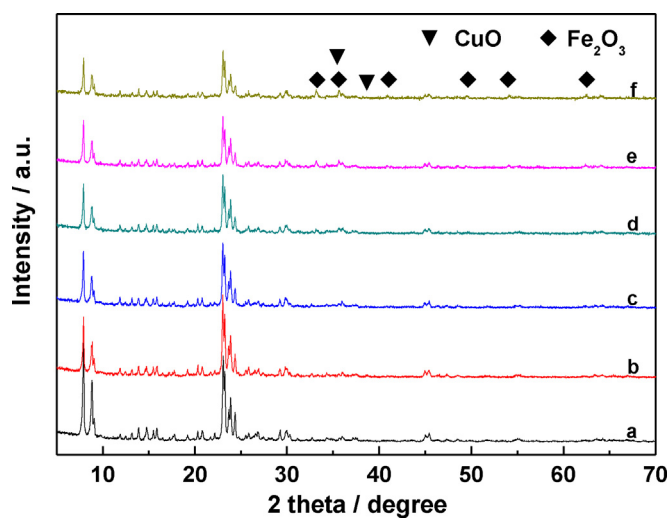


Fig. 3. XRD patterns of pure HZSM-5 (a); Cu₄/ZSM-5 (b); Fe₂-Cu₄/ZSM-5 (c); Fe₄-Cu₄/ZSM-5 (d); Fe₆-Cu₄/ZSM-5 (e); Fe₈-Cu₄/ZSM-5 (f).

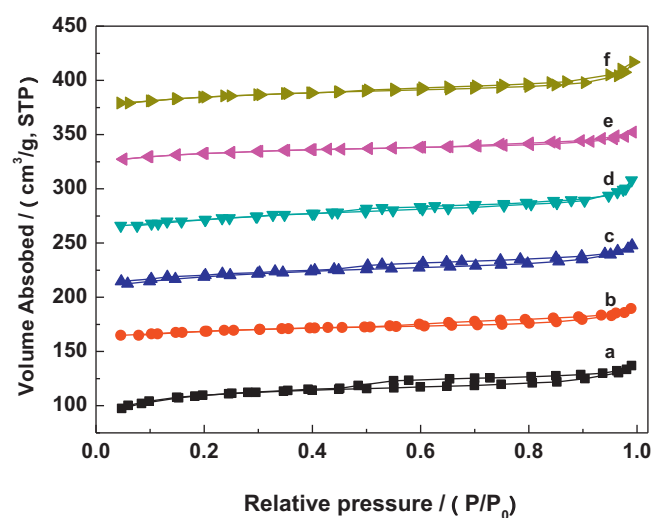


Fig. 4. Nitrogen adsorption–desorption isotherms of pure HZSM-5 (a); Cu₄/ZSM-5 (b); Fe₂-Cu₄/ZSM-5 (c); Fe₄-Cu₄/ZSM-5 (d); Fe₆-Cu₄/ZSM-5 (e); Fe₈-Cu₄/ZSM-5 (f).

3.2.2. The results of BET

Nitrogen adsorption–desorption isotherms for pure HZSM-5, Cu₄/ZSM-5 and Fe_x-Cu₄/ZSM-5 catalysts are shown in Fig. 4. The isotherm for pure HZSM-5 sample is similar to a type-I isotherm characteristic of microporous materials [25], and has a narrow pore size distribution with an average pore diameter of 2.37 nm (see Table 1). The adsorption–desorption isotherm shape remains unchanged after the modification of HZSM-5 with copper and iron. However, copper incorporation leads to a dramatic decrease in BET surface area and micro-pore volume, from 358.0 m² g^{−1} and 0.162 cm³ g^{−1} to 272.5 m² g^{−1} and 0.129 cm³ g^{−1}, for HZSM-5 and Cu₄/ZSM-5, respectively. It is because that copper species cover

Table 1

Physicochemical properties of pure ZSM-5, Cu/ZSM-5 and Fe-Cu/ZSM-5 samples.

Samples	S _{BET} ^a (m ² g ^{−1})	V _{mic} ^b (cm ³ g ^{−1})	Average pore diameter (nm)
Pure ZSM-5	358.0	0.162	2.37
Cu ₄ /ZSM-5	272.5	0.129	2.44
Fe ₂ -Cu ₄ /ZSM-5	302.7	0.135	2.50
Fe ₄ -Cu ₄ /ZSM-5	296.9	0.131	2.68
Fe ₆ -Cu ₄ /ZSM-5	268.4	0.122	2.36
Fe ₈ -Cu ₄ /ZSM-5	271.0	0.121	2.65

^a Calculated by BET method.

^b Calculated by *t*-plot method.

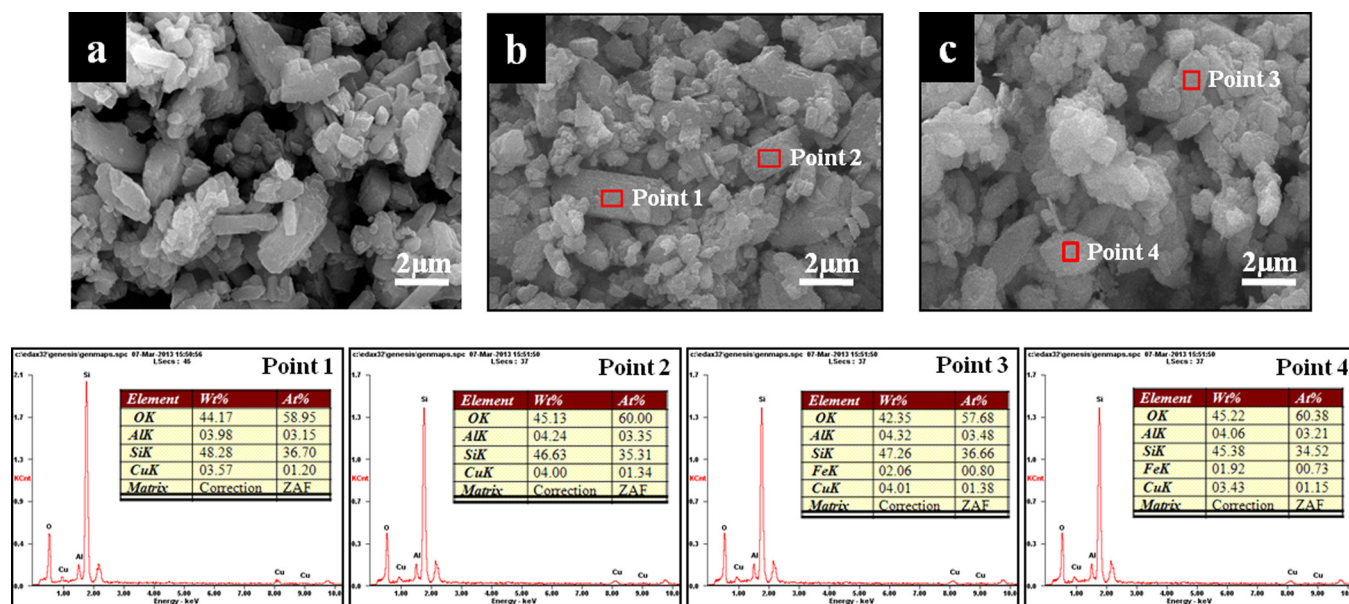


Fig. 5. SEM images and EDX analyses for pure HZSM-5 (a); Cu₄/ZSM-5 (b); Fe₂-Cu₄/ZSM-5 (c).

the external surface of ZSM-5 and clog the micropores of ZSM-5 support. However, as iron was introduced the BET surface areas and pore volumes increase to 302.7 m² g⁻¹ and 0.135 cm³ g⁻¹ for Fe₂-Cu₄/ZSM-5. It indicated that the strong interaction between iron and copper species prevented Cu species aggregation which would clog the micropores of carriers. The surface area and pore volume of catalyst were increased. The strong interaction might be attributed to the formation of highly disperse Fe-Cu nanocomposites.

3.2.3. The results of SEM

The SEM image in Fig. 5a shows that pure HZSM-5 sample is composed of irregularly localized, distinct edged and bright polycrystalline aggregates within the regular geometry. This is virtually unchanged in the morphology of zeolite samples after copper and iron incorporation. When a second metal, i.e., Fe, is loaded on the sample (Fig. 5c), ZSM-5 grain surfaces become rougher and are coated with a “layer”, probably consisting of irregular nano-sized species, i.e., Fe-Cu nanocomposites. The EDX results collected from different regions (Point 1 and Point 2 in Fig. 5b; Point 3 and Point 4 in Fig. 5c) give similar compositions, average copper loadings of 3.57–4.00 wt% are detected for Cu₄/ZSM-5 sample, and average copper loadings of 3.43–4.01 wt% and average iron loadings of 1.92–2.06 wt% are detected for the Fe₂-Cu₄/ZSM-5 sample, in good agreement with the initial nominal loading amounts.

3.2.4. The results of TEM

Distributions of the copper and iron species were further confirmed by the means of HAADF-STEM experiment combining with EDS element-mapping analysis. Fig. 6a shows the HAADF-STEM images of Fe₂-Cu₄/ZSM-5 together with the elemental mapping images for O, Cu, and Fe in the same region. In the HAADF-STEM image, small particles imaged in the bright contrast were observed on the ZSM-5 support and few large crystalline species were observed, suggesting the highly dispersed nature of copper and iron species on the supports. From Cu and Fe elemental mapping image, it is clear that copper and iron signals show the similar distributions, which corresponds to the bright contrast in the HAADF image. The homogeneity of copper and iron species in the Fe₂-Cu₄/ZSM-5 catalyst is also confirmed by the results of EDS line scanning, as shown in Fig. 6b and c. The intensity profiles of Cu and Fe signals

follow a similar trend, indicating that the dispersion of Cu and Fe is homogeneous. Based on the above results, it is reasonable to conclude that nanoparticles on Fe₂-Cu₄/ZSM-5 may exist in the state of Fe-Cu nanocomposites.

Fig. 6d and e shows the TEM images and size distribution of supported CuO nanoparticles of Cu₄/ZSM-5 and Cu₆/ZSM-5. Fig. 6f and g shows the TEM images and size distribution of Fe-Cu nanocomposites of Fe₂-Cu₄/ZSM-5 and Fe₄-Cu₄/ZSM-5. The faint background belongs to zeolite support and the dark spots are CuO nanoparticles or Fe-Cu nanocomposites. However, the presence of CuO was not detected by XRD due to the small size of the crystallites (<4 nm) and their high dispersion. The TEM image in Fig. 6d shows interference fringes of the ZSM-5 crystal structure. The CuO nanoparticles or Fe-Cu nanocomposites on the supports show a uniform distribution and small particle sizes. The mean diameters were by statistic analysis of more than 100 particles in TEM images. The average particle size is 3.48 nm for CuO on Cu₄/ZSM-5 (Fig. 6d), 2.35 nm for Fe-Cu nanocomposites on Fe₂-Cu₄/ZSM-5, and 3.13 nm for Fe-Cu nanocomposites on Fe₄-Cu₄/ZSM-5. This indicates that iron addition influences the dispersion of copper species and reduces the aggregation of copper species. However, the average particle size of Fe-Cu nanocomposites on Fe_x-Cu₄/ZSM-5 would slightly grow larger when iron addition was more than 2 wt%. Therefore, Fe₄-Cu₄/ZSM-5 (Fig. 6d) with almost equal average size of 3.13 nm and Cu₄/ZSM-5 (Fig. 6a) with an average size of 3.4 nm show almost the same dispersity. But it should be noted that the nanoparticles on Cu₄/ZSM-5 only contain copper species, whereas that on Fe₄-Cu₄/ZSM-5 contain both copper and iron species. In comparison, it is reasonable to conclude that the presence of iron also can reduce the aggregation of copper species. In contrast, for Cu₆/ZSM-5, the average CuO size is 4.11 nm, and the size distribution is relatively broad (Fig. 6e), suggesting a large aggregation of CuO particles.

3.2.5. The results of FT-IR

FT-IR spectra of pure HZSM-5, Cu₄/ZSM-5 and Fe_x-Cu₄/ZSM-5 samples are shown in Fig. 7. The spectra of all samples exhibit similar structure characteristics. The band at 450 cm⁻¹ expresses the vibration of TO₄ units, and that at 550 cm⁻¹ is attributable to the vibration of five-membered oxygen rings. The bands of Fe_x-Cu₄/ZSM-5 catalysts do not show the characteristic framework

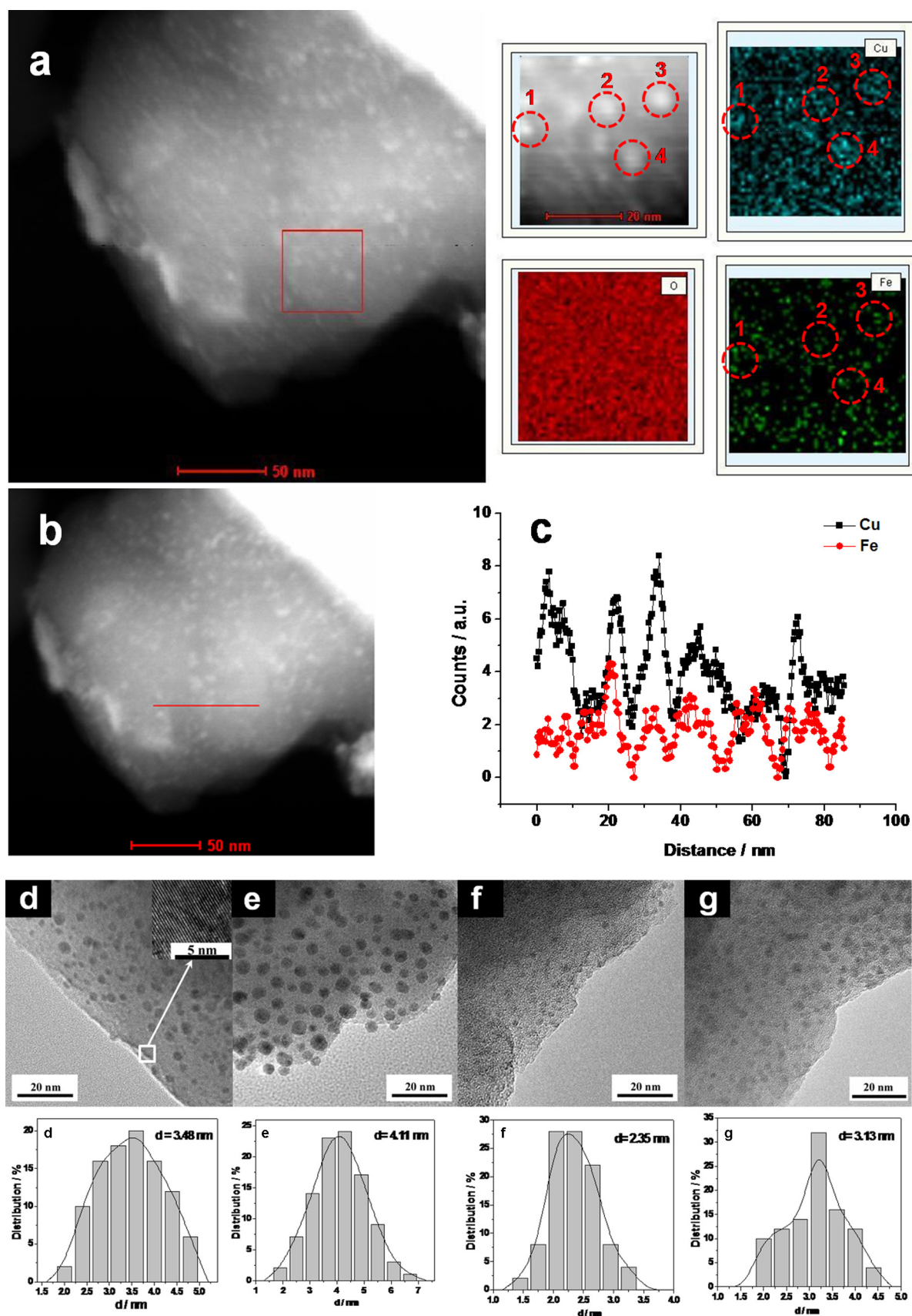


Fig. 6. HAADF-STEM image and EDS elemental mapping and line analyses (a–c) of $\text{Fe}_2\text{-Cu}_4/\text{ZSM-5}$ catalyst. TEM images, and size distribution of CuO nanoparticles of $\text{Cu}_4/\text{ZSM-5}$ (d); $\text{Cu}_6/\text{ZSM-5}$ (e); and TEM images, size distribution of Fe–Cu nanocomposite oxide of $\text{Fe}_2\text{-Cu}_4/\text{ZSM-5}$ (f); $\text{Fe}_4\text{-Cu}_4/\text{ZSM-5}$ (g).

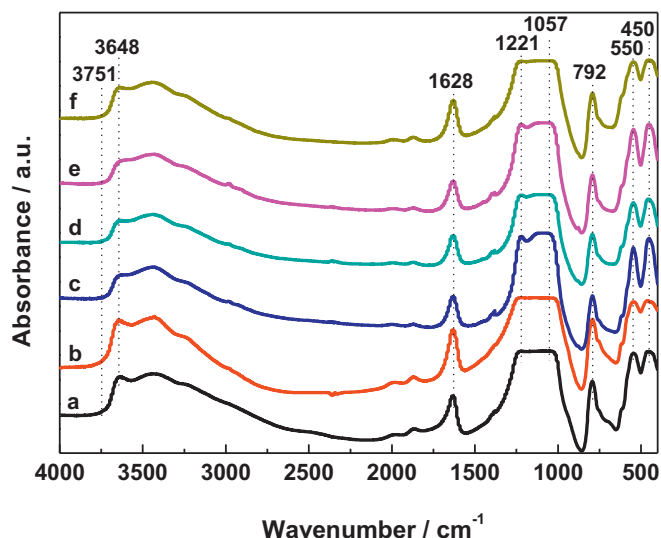


Fig. 7. FT-IR absorbance spectra of pure HZSM-5 (a); Cu₄/ZSM-5 (b); Fe₂-Cu₄/ZSM-5 (c); Fe₄-Cu₄/ZSM-5 (d); Fe₆-Cu₄/ZSM-5 (e); Fe₈-Cu₄/ZSM-5 (f).

band at 710–700 cm⁻¹ suggesting extra-framework iron [26]. The band close to 792 cm⁻¹ is assigned to the symmetric stretching and deformation modes of the Si–O–Si framework, and the band at around 1057 cm⁻¹ corresponds to the asymmetric stretching vibration of Si–O–Si. The bands in the 918–923 cm⁻¹ range due to Cu²⁺ (isolated and oxygen bridged) perturbations of asymmetric internal zeolite stretching vibrations, and the bands at 591 and 628 cm⁻¹ are associated with Cu–O vibrations in bulk CuO [26], those are not observed. Sachtler and coworkers [27] found that these bands are highly sensitive to pretreatment or experimental conditions. The intense band at 1221 cm⁻¹ for all samples is associated with the asymmetric internal tetrahedron vibrations of SiO₄. The broad peak in the 3000–3700 cm⁻¹ range and a band at around 1628 cm⁻¹ for all spectra are due to the stretching vibrations of hydrogen-bonded silanols and water, and to the deformation vibration of water, respectively. The band at 3648 cm⁻¹ for the samples attributes to bridging hydroxyl groups (Si–OH)–Al, which is associated with Brønsted acid sites. The 3751 cm⁻¹ absorption band is attributed to the stretching vibrations of terminal silanol groups (Si–OH). For Fe_x-Cu₄/ZSM-5 catalysts, as the iron content increases, the peak intensity reduces slightly, indicating that partial iron ions are anchored on the bridging oxygen of Si–OH–Al groups.

3.2.6. The results of UV–vis DRS

UV–vis DRS spectroscopy was applied to understand the nature and coordination of copper and iron species in the samples. Fig. 8 shows the UV–vis absorption spectra of pure HZSM-5, Cu₄/ZSM-5 and Fe_x-Cu₄/ZSM-5 catalysts. The bands at about 225, 280, and 361 nm are assigned to zeolite ZSM-5. For Cu₄/ZSM-5 sample, several bands appear, a broad band appears between 540 nm and 800 nm, centered at about 750 nm and a narrow one located at about 200 nm. The first one is assigned to d–d transitions of Cu²⁺ ions in a pseudo-octahedral ligand oxygen environment, which is due to copper species in the extra-framework position (dispersed CuO nanoparticles). The second one at about 200 nm, is assigned to the charge transfer band related to O → Cu transition from lattice oxygen to isolated Cu²⁺ ions [28].

In addition, Fe_x-Cu₄/ZSM-5 samples have two absorption peaks at about 250 and 293 nm that are seen as Fe-ZSM-5-type structures. It is important to note that assignments of UV–vis absorption for Fe-ZSM-5 have remained a subject of discussion in literature. The absorption of the UV region (<450 nm) may be due to

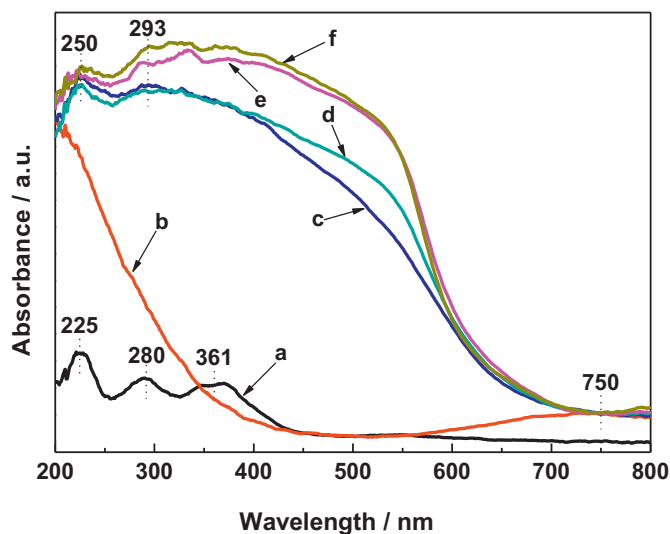


Fig. 8. UV–vis DRS spectra of pure HZSM-5 (a); Cu₄/ZSM-5 (b); Fe₂-Cu₄/ZSM-5 (c); Fe₄-Cu₄/ZSM-5 (d); Fe₆-Cu₄/ZSM-5 (e); Fe₈-Cu₄/ZSM-5 (f).

O → Fe³⁺ ligand-to-metal charge-transfer (LMCT) transitions [29]. Schwidder et al. [18] assigned the band at <300 nm to isolated Fe³⁺, the band at 300–400 nm to oligomeric clusters, and the band at >400 nm to large Fe₂O₃ particles. The absorption in >450 nm region is due to d–d transition of α-Fe₂O₃, a unique phenomenon to α-Fe₂O₃ [30]. Lu et al. [30] assign the bands near 670 and 560 nm to ground state, first excited state, and second excited state configurations of high-spin Fe³⁺. They also note that the band near 560 nm is strongest and its actual position depends on the particle size of α-Fe₂O₃. Thus the absorption band at 250 and 293 nm of Fe_x-Cu₄/ZSM-5 may be assigned to O → Fe³⁺ LMCT transitions and/or oligomeric clusters (e.g., [HO–Fe–O–Fe–OH]²⁺). The absorption bands in >450 nm region are assignable to α-Fe₂O₃. The UV–vis results clearly indicate that the nature and distribution of the iron species change with increasing iron loading amount for Fe_x-Cu₄/ZSM-5 catalysts. The bands are broadened and shifted towards higher wavelengths as the iron content increased. However, it is difficult to quantify these species because the extinction coefficients of each species are not known and several peaks overlap complexity.

The results of UV–vis indicate that the bimetallic Fe–Cu nanocomposites catalysts seem to contain several types of active sites that could be associated with copper and iron species. Cu species were in form of highly dispersed CuO nanoparticles and isolated Cu²⁺ ions. Meanwhile, three types of Fe species exist in Fe–Cu nanocomposites on Fe_x-Cu₄/ZSM-5 catalysts, aggregated α-Fe₂O₃ species, Fe_xO_y oligomer and oxo-Fe³⁺. Furthermore, the copper structures: copper dimer [31], chainlike (Cu–O)_n complex [32], bis (μ-oxo) dicopper core [33] and even small copper oxides clusters Cu_nO_y [34] are taken to be active in the majority of DeNO_x processes. Our studies on NH₃-SCR over the Cu₄/ZSM-5 and Fe_x-Cu₄/ZSM-5 catalysts are well consistent with these conclusions. From the results of UV–vis and activity test, we can speculate that NH₃-SCR is promoted both by oxo-Fe³⁺ and oligomeric Fe oxo species, and the latter has a greater intrinsic activity [35]. Moreover, for Fe₆-Cu₄/ZSM-5 catalysts, the decline of NO conversion above 375 °C was most likely due to the considerable oxidation activity of the Fe oxo clusters, i.e., aggregated α-Fe₂O₃ species. NH₃ oxidation activity increased dramatically above 4 wt% Fe loading amount, and the active temperature range became narrow. Thus, chemical promotion combined with optimal fraction of copper and iron active species in the Fe–Cu nanocomposites might be efficient route to further enhance NH₃-SCR activity.

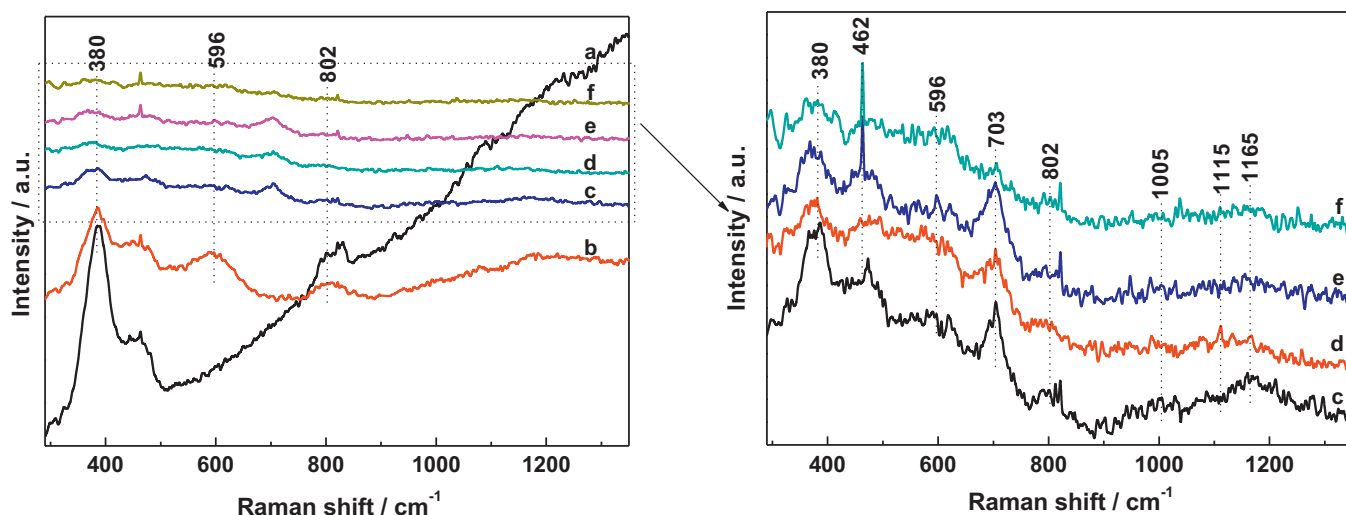


Fig. 9. Raman spectra with excitation at 325 nm of pure HZSM-5 (a), Cu₄/ZSM-5 (b), Fe₂-Cu₄/ZSM-5 (c), Fe₄-Cu₄/ZSM-5 (d), Fe₆-Cu₄/ZSM-5 (e) and Fe₈-Cu₄/ZSM-5 (f).

3.2.7. The results of Raman spectroscopy

The Raman spectra of pure HZSM-5, Cu₄/ZSM-5 and Fe_x-Cu₄/ZSM-5 catalysts with the excitation line at 325 nm are shown in Fig. 9. The bands at 380 and 802 cm⁻¹ are assigned to the five-membered building unit of the MFI-structured zeolite and the framework symmetric stretching vibration of ZSM-5, respectively [36]. The intensities of the bands related to MFI decrease for Cu₄/ZSM-5 and Fe_x-Cu₄/ZSM-5 catalysts. XRD analyses (Fig. 3) indicate that the structures are not damaged. The decrease of the MFI-related vibrational bands may be partially attributed to the perturbation of the zeolite vibrations in the presence of extra-framework copper and iron species. Another possible reason relates to the scattering nature of Raman spectroscopy which makes it a surface-sensitive technique. With copper and iron addition, the color change of the samples (vide infra) may lead to the partial masking of the zeolite-related signals.

In Cu₄/ZSM-5 catalyst, in addition to typical bands of HZSM-5, additional band is at 596 cm⁻¹ which might correspond to stretching vibration mode of Cu-O bonds. In Fe_x-Cu₄/ZSM-5 catalysts, the band at 462 cm⁻¹ could be tentatively assigned to Fe-O-Fe symmetric stretching modes of a bi-nuclear cationic Fe species [37] and their intensities increase after the iron loading. Additional bands at 1016, 1115, and 1165 cm⁻¹ may be ascribed to the asymmetric stretching modes of Fe³⁺ surrounded by oxygen anions of the framework [38], in accordance with the UV-vis results. A further increase in iron loading amounts results in the reduction of the intensities of the bands at 1005, 1115 and 1165 cm⁻¹. This suggests that extra-framework Cu leads to in a clustering of isolated iron ions into bi- and oligo-nuclear iron cluster, in accordance with UV-vis results. In addition, for Fe_x-Cu₄/ZSM-5 catalysts, a new band appears around 703 cm⁻¹. It is found that Fe-Cu nanocomposites tend to become better dispersed with decreasing Fe content. Concomitantly, the Raman band at around 703 cm⁻¹ becomes more intense, suggesting that it should be related to a highly dispersed form of Fe.

3.2.8. The results of NH₃-TPD

Temperature-programmed desorption of ammonia was carried out to determine the strength and amount of different acid sites. The NH₃-TPD profiles from pure HZSM-5, Cu₄/ZSM-5 and Fe_x-Cu₄/ZSM-5 catalysts are displayed in Fig. 10. Two desorption peaks at around 268 and 559 °C are observed for parent HZSM-5, corresponding to the weak and the strong acid sites,

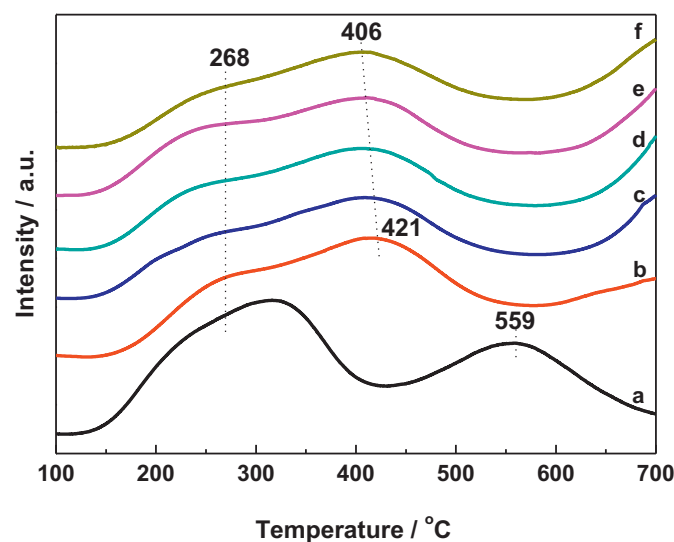


Fig. 10. NH₃-TPD curves of pure HZSM-5 (a); Cu₄/ZSM-5 (b); Fe₂-Cu₄/ZSM-5 (c); Fe₄-Cu₄/ZSM-5 (d); Fe₆-Cu₄/ZSM-5 (e); Fe₈-Cu₄/ZSM-5 (f).

respectively. The desorption peak centered at the lower temperature is attributable to physisorbed NH₃ or ammonium species, while the peak at the higher temperature is assigned to NH₃ strongly adsorbed at the strong Brønsted acid sites [39]. For Cu₄/ZSM-5 and Fe_x-Cu₄/ZSM-5 catalysts, the intensity of the higher temperature peaks (~400 °C) is lower than that of HZSM-5, because the Brønsted acid protons were substituted for Cu²⁺ and/or Fe³⁺. Moreover, the peak temperature of these peaks is also shifted slightly towards a lower temperature with increasing iron loading amounts, indicating that the decreasing strength of Brønsted acid sites. This gradual temperature shift may be due to a decrease in the acid site density, which hamper the readsorption of ammonia on the acid sites during its desorption [40]. In addition, a new and distinct NH₃ desorption peak appeared at a high temperature of >580 °C for Cu₄/ZSM-5 and Fe_x-Cu₄/ZSM-5 catalysts, indicating the creation of the stronger acid sites, which might be due to strong Lewis acid sites [41]. It indicates that the strong Lewis acid sites can originate from the high dispersion of copper and iron species.

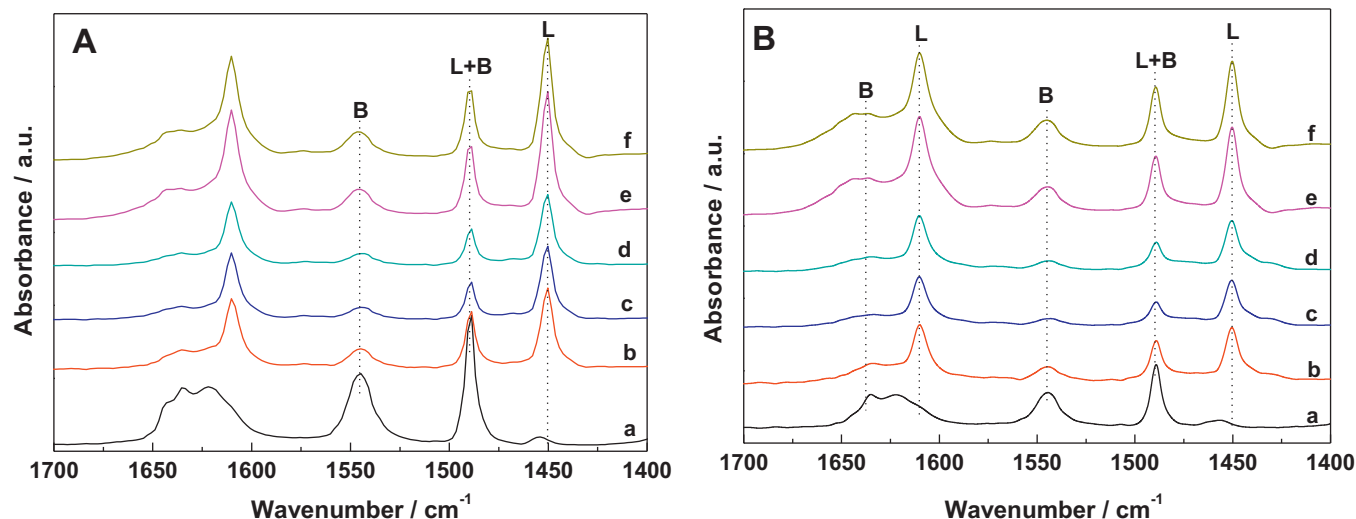


Fig. 11. FT-IR spectra of pyridine adsorbed on pure HZSM-5 (a), Cu₄/ZSM-5 (b), Fe₂-Cu₄/ZSM-5 (c), Fe₄-Cu₄/ZSM-5 (d), Fe₆-Cu₄/ZSM-5 (e) and Fe₈-Cu₄/ZSM-5 (f) after degassing at 200 °C (A) and 350 °C (B).

3.2.9. The results of Py-IR

A good SCR catalyst should have proper acid sites (Brønsted vs. Lewis). Brønsted acid was necessary to bind and disperse the metal ions, which might also prevent the aggregation of exchanged metal ions. Both the weak and strong Lewis acid sites in the zeolite framework might act as an adsorption site for NH₃ and therefore as a reservoir of the reductant [42]. The spectra of pyridine adsorbed pure HZSM-5, Cu₄/ZSM-5 and Fe_x-Cu₄/ZSM-5 catalysts after outgassing at different temperatures are shown in Fig. 11. The spectra of pyridine adsorbed on different catalysts displayed bands at around 1450 and 1610 cm⁻¹, which are assigned to pyridine coordinated to Lewis acid sites, and the bands at around 1545 and 1637 cm⁻¹ attributing to pyridine coordinated to Brønsted acid sites. The band at about 1495 cm⁻¹ can be assigned to pyridine coordinated to Lewis and Brønsted acid sites. The spectrum of HZSM-5 is dominated by the signal of PyH⁺ although some Lewis acid sites (1455 cm⁻¹) resulting from available Al³⁺ as well. Upon introduction of copper, the center of the L-Py band shifts to lower wavenumber (1450 cm⁻¹), and the ratio between Brønsted and Lewis acid sites (PyH⁺/L-Py) changes dramatically. After degassing at 200 °C, in Cu₄/ZSM-5 the introduction of copper into HZSM-5 led to a decrease of Brønsted acid sites (1540 cm⁻¹ band), which was expected as the acid sites are replaced by the exchanged copper species. Exchanged copper species in turn seems to generate additional Lewis acid sites (1450 and 1610 cm⁻¹ bands). It can be seen that in the Fe-added samples the Lewis and Brønsted acid sites are more abundant than those in Cu₄/ZSM-5. This distinction is less notable for the amounts of medium and strong acid sites (after degassing at 350 °C).

3.2.10. The results of H₂-TPR

To gain a better understanding of the redox properties of the catalysts, the H₂-TPR of pure HZSM-5, Cu₄/ZSM-5 and Fe_x-Cu₄/ZSM-5 catalysts were measured (Fig. 12). No clear H₂ consumption signal was detected for pure HZSM-5. The TPR results show that multiple copper and iron species coexist in the samples and the amount of each species varies with different Fe contents. Definitely assigning H₂ consumption peaks to various copper and iron species was a difficult task, and we relied heavily on the extensive literature for copper and iron species in zeolitic materials.

For Cu₄/ZSM-5 sample, the H₂ consumption signals from 200 to 400 °C are most likely related to the copper active species for SCR reaction. Praliaud et al. [43] reported that two types of cupric

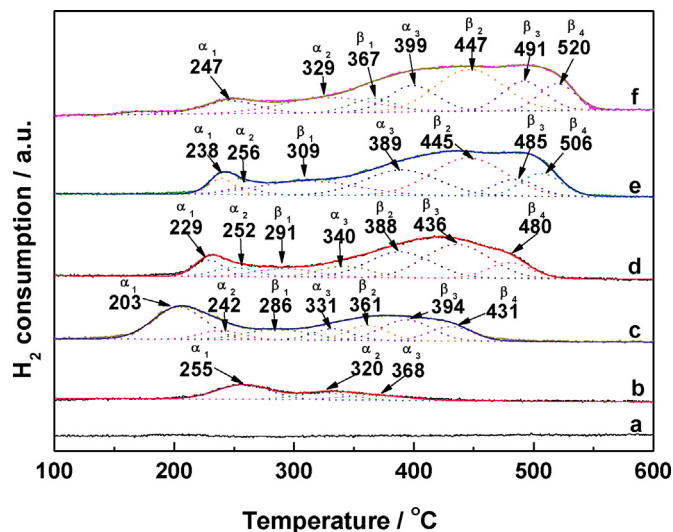


Fig. 12. TPR profiles of pure HZSM-5 (a); Cu₄/ZSM-5 (b); Fe₂-Cu₄/ZSM-5 (c); Fe₄-Cu₄/ZSM-5 (d); Fe₆-Cu₄/ZSM-5 (e); Fe₈-Cu₄/ZSM-5 (f).

ions located on the HZSM-5, isolated Cu²⁺ ions at exchange sites and copper oxides. Nanba et al. [44] found that both these cupric species were reduced by H₂ at temperatures below 330 °C and assigned the peak at 250 °C as the reduction of isolated Cu²⁺ located in Cu/ZSM-5 catalyst. A peak fitting of the profiles was performed in order to identify the temperature of the different reduction events. Thus, by means of the peak fitting, we assign the peak at around 255 °C (α₁) to the reduction of isolated Cu²⁺ ions and the peak at around 320 °C (α₂) to the reduction of nano-sized CuO crystallites [45]. The H₂ consumption peak at around 368 °C (α₃) is attributed to the reduction of Cu⁺ to Cu⁰, and the Cu⁺ is formed from the reduction of isolated Cu²⁺ and nano-sized CuO crystallites.

For Fe_x-Cu₄/ZSM-5 catalysts, at the lower temperature (≤400 °C), the peaks correspond to the combined reduction of Cu²⁺ and/or nano-sized CuO crystallites to Cu⁰ (α₁, α₂, α₃) and Fe³⁺ and/or α-Fe₂O₃ to Fe^{(3-δ)+} (β₁) with intermediate valence as that in Fe₃O₄ and then to Fe²⁺ (β₂) [21]. At the higher temperature (>400 °C), the peaks represent the partial reduction of Fe²⁺ to Fe⁰ (β₃, β₄). The results of H₂-TPR indicate that the reduction peaks of copper species shift to a slightly lower temperature, suggesting

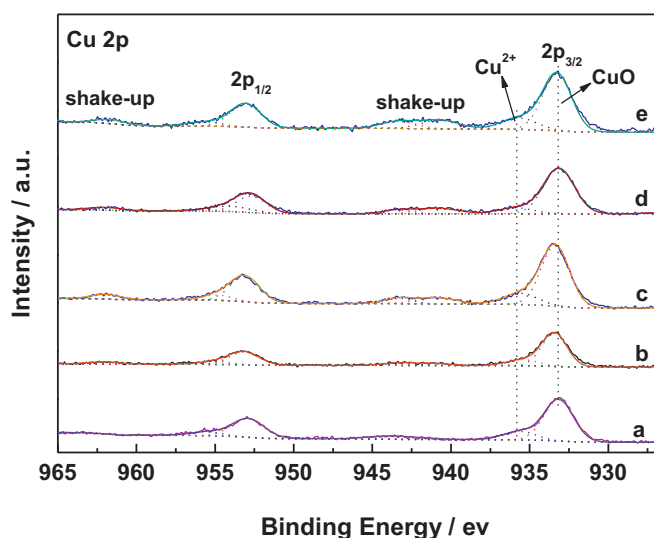


Fig. 13. XPS results of Cu 2p of Cu₄/ZSM-5 (a); Fe₂-Cu₄/ZSM-5 (b); Fe₄-Cu₄/ZSM-5 (c); Fe₆-Cu₄/ZSM-5 (d); Fe₈-Cu₄/ZSM-5 (e).

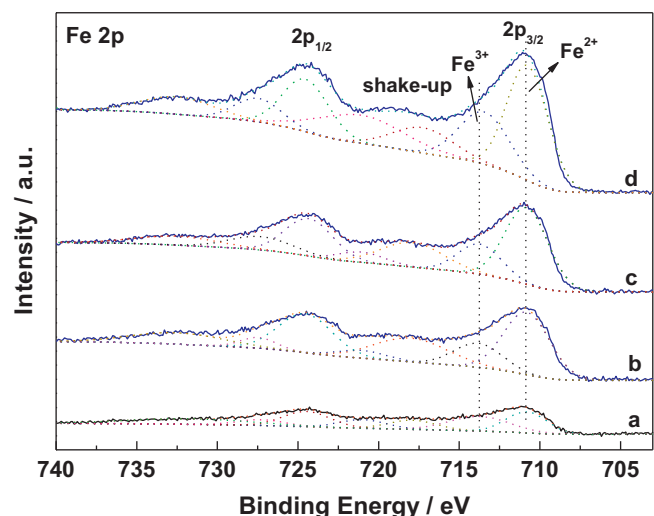


Fig. 14. XPS results of Fe 2p of Fe₂-Cu₄/ZSM-5 (a); Fe₄-Cu₄/ZSM-5 (b); Fe₆-Cu₄/ZSM-5 (c); Fe₈-Cu₄/ZSM-5 (d).

that the interaction between iron and copper species. The improvement in the reduction of active species is considered as one reason for the excellent activity of Fe_x-Cu₄/ZSM-5 catalysts.

3.2.11. The results of XPS

In order to understand the nature of the interaction between the two metal species, Cu₄/ZSM-5 and Fe_x-Cu₄/ZSM-5 samples are investigated using the XPS technique. Fig. 13 exhibits the XPS results of Cu 2p for the Cu₄/ZSM-5 and Fe_x-Cu₄/ZSM-5. The Cu 2p_{3/2} signal is composed of two peaks at 933.4 eV and 935.6 eV, where the former is assigned to the presence of CuO species [46] and the latter due to Cu²⁺ ion being coordinated to superficial oxygen atoms of the zeolite [47]. The Cu 2p_{3/2} and Cu 2p_{1/2} peaks are accompanied by distinct shakeup satellites at about B.E. of 942 and 962 eV. These characteristic satellites can be attributed to the charge transfer between the transition metal 3d and surrounding ligand oxygen 2p orbitals [48].

Fig. 14 shows the XPS spectra of Fe 2p for Fe_x-Cu₄/ZSM-5 catalysts. The characteristic peak of Fe 2p_{3/2} is located at about 711 eV and Fe 2p_{1/2} at 724 eV. From the deconvolution of the XPS spectra of

Table 2

Surface composition and oxidation state of Fe 2p species over Fe_x-Cu₄-ZSM-5 catalysts from XPS analyses.

Sample	Fe species		
	Fe ²⁺	Fe ³⁺	R ^a
Fe ₂ -Cu ₄ /ZSM-5	49.8	50.2	0.992
Fe ₄ -Cu ₄ /ZSM-5	71.7	28.3	2.534
Fe ₆ -Cu ₄ /ZSM-5	70.3	29.7	2.367
Fe ₈ -Cu ₄ /ZSM-5	64.4	35.6	1.809

^a Determined by the Fe species ratio of the Fe²⁺/Fe³⁺.

Fe 2p_{3/2}, two distinct bands which centered at 710.9 and 713.8 eV are observed. These values are close to the range of Fe 2p_{3/2} binding energies of iron in FeO and Fe₂O₃ [49], respectively, indicating that the iron in our samples is present both as Fe²⁺ and Fe³⁺. Furthermore, a shakeup satellite is associated with the Fe 2p_{3/2} peak. The satellite is located approximately 7 eV higher in binding energy than the main Fe 2p_{3/2} peak.

4. Discussion

In bicomponent nanocomposite catalysts, the addition of a second metal is found to restrain the aggregation of monometals [50]. The results of HAADF-STEM image and EDS elemental mapping and line analyses show that iron and copper species formed Fe-Cu nanocomposites on the surface of Fe_x-Cu₄/ZSM-5 catalysts. In contrast to monometallic Cu₄/ZSM-5 catalyst, iron plays a successive role in influencing the dispersion of copper species, and then influences the activity of Cu₄/ZSM-5 catalyst. At the microscopic level, the effect of iron addition on copper dispersion may be due to the anchoring of Cu²⁺ on the iron phase leading to the formation of small copper crystallites stabilized by iron species. Several early studies showed that, in bimetallic-based systems, the less reducible metal inhibits the aggregation of the easily reduced metal [51]. The reason is that the less reducible metals act as anchors for more reducible metals. This is well established for noble metals interacting with iron in bimetallic catalysts [52]. Similar conclusions have been reached with the Fe-Cu system. Well dispersed particles with narrow size distribution were evidenced in CuFeO_x catalysts prepared by co-precipitation [53]. Intimately mixed CuO and Fe₂O₃ crystallites were also found in supported bimetallic Fe-Cu catalysts [54].

The electronic properties of bimetallic nanocomposite catalysts usually differ from those of monometallic nanocomposite catalysts and significantly vary as a function of the composition. The results of XPS (Fig. 13) show that the B.E. of Fe₂-Cu₄/ZSM-5 (932.4 eV) and Fe₄-Cu₄/ZSM-5 (932.5 eV) for Cu 2p_{3/2} present a slower blue shift compared with those of Cu₄/ZSM-5 (932.2 eV), Fe₆-Cu₄/ZSM-5 (932.1 eV) and Fe₈-Cu₄/ZSM-5 (932.2 eV), indicating the weak interaction between the Fe and Cu species in these two catalysts and the better dispersion of CuO on the zeolite. The results of XPS also suggest that the value of R^a (the Fe species ratio of Fe²⁺/Fe³⁺) increases from 0.992 (Fe₂-Cu₄/ZSM-5) to 2.534 (Fe₄-Cu₄/ZSM-5) in Table 2. The increasing of Fe²⁺ contents contributes to the interaction between iron and the surrounding atoms, i.e., Cu. Furthermore, copper species partially incorporate into the iron oxide matrix and modify the electronic properties of the iron oxide structure [55], which causes the imperfect structure of iron oxide, and promotes the formation of oxygen vacancies through an oxygen vacancies compensation mechanism [56]. When every two Cu²⁺ ions replacing Fe³⁺ ions, one oxygen vacancy may be formed to balance the charge. Since oxygen mobility increases with oxygen vacancy concentration, it is expected that the catalysts containing suitable amount of doped iron enhance the redox ability.

The second metal introduction can create new acid sites compared with monometal catalyst. The results of NH_3 -TPD show that the exchange of acidic protons by Fe cations would give a rise to new acid-base and redox properties. When Fe cations were introduced to $\text{Cu}_4/\text{ZSM-5}$, Fe^{3+} would substitute the H proton of bridging hydroxyls (Brønsted acid sites) on zeolite, meanwhile Lewis acid sites of $\text{Cu}_4/\text{ZSM-5}$ catalyst were inhibited and covered by the iron species. In addition, new Lewis acid sites appeared which mainly originated from the high dispersion of iron species. The pyridine adsorption study confirms that the Fe ions have Lewis-character. However, it is surprising that the intensity of the Brønsted bands increases in $\text{Fe}_x\text{-Cu}_4/\text{ZSM-5}$ compared with $\text{Cu}_4/\text{ZSM-5}$, it may be due to a $\text{Fe}^{3+}(\text{OH})$ group on a site that is abundant in Fe–Cu nanocomposites. According to the results of UV–vis and UV-Raman, $\text{Fe}_x\text{-Cu}_4/\text{ZSM-5}$ contain both isolated and oligomeric Fe species, OH groups associated with these Fe species might be candidates for the Brønsted acid sites of moderate acidity that give rise to the extra intensity in $\text{Fe}_x\text{-Cu}_4/\text{ZSM-5}$.

The redox properties of the catalyst are an important factor for determining the extent of NO conversion in NH_3 -SCR. H_2 -TPR results indicated that the interaction between iron and copper species could also change the redox ability of $\text{Fe}_x\text{-Cu}_4/\text{ZSM-5}$ catalysts. The reduction peaks of copper and iron species were shifted with the change of iron addition amount. The reason is that iron and copper species in Fe–Cu nanocomposites were well mixed and interacted, the nature of copper and iron species was changed, and then caused a lower reduction temperature of the supported active species [57]. Moreover, the shift to lower temperature in the TPR profile of $\text{Fe}_x\text{-Cu}_4/\text{ZSM-5}$ catalysts also depends on the dispersity of active component and interaction between metal and support.

The second metal iron addition can promote the $\text{Cu}_4/\text{ZSM-5}$ catalyst with a more wide activity temperature window. Metal dispersion is one of the factors that affect the catalytic activity of supported metal catalysts. Thus, the well dispersed Fe–Cu nanocomposites on the surface of the $\text{Fe}_x\text{-Cu}_4/\text{ZSM-5}$ catalysts are believed to be useful for its high NH_3 -SCR activity at high temperatures compared with $\text{Cu}_4/\text{ZSM-5}$ catalyst. In addition, the acidity of the zeolites is one of the important parameter that determines the extent of NO_x reduction with ammonia over zeolite-based catalysts [58]. However, in our study, $\text{Fe}_4\text{-Cu}_4/\text{ZSM-5}$ catalyst showed weaker acidity compared with HZSM-5 , $\text{Fe}_6\text{-Cu}_4/\text{ZSM-5}$ and $\text{Fe}_8\text{-Cu}_4/\text{ZSM-5}$ catalysts. It indicates that the iron and copper active sites may be more important than the acidity for SCR reaction over $\text{Fe}_x\text{-Cu}_4/\text{ZSM-5}$ catalysts. This result is in line with the finding of Brandenberger et al. [42], who thought that acidity of Fe–ZSM-5 catalyst was not a crucial factor for high activity. Meanwhile, the catalytic activity of $\text{Fe}_x\text{-Cu}_4/\text{ZSM-5}$ catalysts should be closely related to the iron with different chemical valence ($\text{Fe}^{2+}/\text{Fe}^{3+}$) and their redox properties, and the improvement in the reduction of Fe and Cu species also plays an important role in the excellent activity of $\text{Fe}_x\text{-Cu}_4/\text{ZSM-5}$ sample.

5. Conclusions

In summary, the catalytic performance of $\text{Cu}_4/\text{ZSM-5}$ catalyst for NH_3 -SCR has been improved by adding iron. When iron loading amount is 4 wt%, a wide activity temperature window of $\text{Fe}_4\text{-Cu}_4/\text{ZSM-5}$ catalyst can be obtained, which exhibited the high NO conversion (>90%) in the wide temperature range (200–475 °C).

The presence of iron may influence the dispersion of copper species. HAADF-STEM image and EDS elemental mapping and line analyses show that iron and copper species formed Fe–Cu nanocomposites on the surface of $\text{Fe}_x\text{-Cu}_4/\text{ZSM-5}$ catalysts. The results of XPS indicate that $\text{Cu } 2p_{3/2}$ presents a slight blue shift and the ratio of $\text{Fe}^{2+}/\text{Fe}^{3+}$ increases when Fe addition is less than or

equal to 4 wt%. The presence of iron also improves the reducibility of copper species.

The results of NH_3 -TPD, Py-IR and activity test indicate that the acidity of catalysts affects SCR reaction activity. However, the well dispersed Fe–Cu nanocomposites and Fe–Cu active sites play a more important role in the NH_3 -SCR reaction. A high ratio of $\text{Fe}^{2+}/\text{Fe}^{3+}$ in Fe–Cu nanocomposites is in favor of NH_3 -SCR reaction due to an increase of the oxygen vacancies. Furthermore, the improvement in the reduction of Fe and Cu species also plays an important role in the excellent activity of $\text{Fe}_x\text{-Cu}_4/\text{ZSM-5}$ sample.

Acknowledgements

We sincerely thank Prof. Junhua Li at Tsinghua University for his helping us to measure the selectivity of N_2 and giving us some discussion. This work was supported by the financially NSFC (21376261, 21173270, 21177160), the 863 program (2013AA065302, 2013AA065302), and China University of Petroleum Fund (LLYJ-2011-39, KYJJ2012-06-31).

References

- [1] J.-O. Barth, A. Jentys, J.A. Lercher, *Ind. Eng. Chem. Res.* 43 (2004) 3097–3104.
- [2] R.H. Harding, A.W. Peters, J.R.D. Nee, *Appl. Catal. A* 221 (2001) 389–396.
- [3] J.H. Li, R.H. Zhu, Y.S. Cheng, C.K. Lambert, R.T. Yang, *Environ. Sci. Technol.* 44 (2010) 1799–1805.
- [4] A. Tomita, T. Yoshii, S. Teranishi, M. Nagao, T. Hibino, *J. Catal.* 247 (2007) 137–144.
- [5] P.G.W.A. Kompio, A. Brückner, F. Hipler, G. Auer, E. Löffler, W. Grünert, *J. Catal.* 286 (2012) 237–247.
- [6] P. Balle, B. Geiger, S. Kureti, *Appl. Catal. B* 85 (2009) 109–119.
- [7] Z.M. Liu, J.H. Li, S.I. Woo, *Energy Environ. Sci.* 5 (2012) 8799–8814.
- [8] J.P. Dunn, P.R. Koppula, H.G. Stenger, I.E. Wachs, *Appl. Catal. B* 19 (1998) 103–117.
- [9] S. Djerad, M. Crocoll, S. Kureti, L. Tifouti, W. Weisweiler, *Catal. Today* 113 (2006) 208–214.
- [10] W.P. Shan, F.D. Liu, H. He, X.Y. Shi, C.B. Zhang, *Catal. Today* 184 (2012) 160–165.
- [11] H.R. Li, D.S. Zhang, P. Maitaray, L.Y. Shi, R.H. Gao, J.P. Zhang, W.G. Cao, *Chem. Commun.* 48 (2012) 10645–10647.
- [12] M. Iwasaki, K. Yamazaki, K. Banno, H. Shinjoh, *J. Catal.* 260 (2008) 205–216.
- [13] D.W. Fickel, E. D'Addio, J.A. Lauterbach, R.F. Lobo, *Appl. Catal. B* 102 (2011) 441–448.
- [14] G. Carja, Y. Kameshima, K. Okada, C.D. Madhusoodana, *Appl. Catal. B* 73 (2007) 60–64.
- [15] H. Sjövall, L. Olsson, E. Fridell, R.J. Blint, *Appl. Catal. B* 64 (2006) 180–188.
- [16] S. Kieger, G. Delahay, B. Coq, B. Neveu, *J. Catal.* 183 (1999) 267–280.
- [17] M.S. Kumar, M. Schwidder, W. Grünert, A. Brückner, *J. Catal.* 227 (2004) 384–397.
- [18] M. Schwidder, M.S. Kumar, K. Klementiev, M.M. Pohl, A. Brückner, W. Grünert, *J. Catal.* 231 (2005) 314–330.
- [19] G.L. Brett, Q. He, C. Hammond, P.J. Miedziak, N. Dimitratos, M. Sankar, A.A. Herzing, M. Conte, J.A. Lopez-Sanchez, C.J. Kiely, D.W. Knight, S.H. Taylor, G.J. Hutchings, *Angew. Chem. Int. Ed.* 50 (2011) 10136–10139.
- [20] H.Z. Chang, X.Y. Chen, J.H. Li, L. Ma, C.Z. Wang, C.X. Liu, J.W. Schwank, J.M. Hao, *Environ. Sci. Technol.* 47 (2013) 5294–5301.
- [21] F.D. Liu, H. He, *J. Phys. Chem. C* 114 (2010) 16929–16936.
- [22] S. Brandenberger, O. Kröcher, A. Tissler, R. Althoff, *Appl. Catal. B* 95 (2010) 348–357.
- [23] J. Wang, T. Yu, X.Q. Wang, G.S. Qi, J.J. Xue, M.Q. Shen, W. Li, *Appl. Catal. B* 127 (2012) 137–147.
- [24] G.S. Qi, R.T. Yang, *Appl. Catal. A* 287 (2005) 25–33.
- [25] F. Bin, C.L. Song, G. Lv, J.N. Song, X.F. Cao, H.T. Pang, K.P. Wang, *J. Phys. Chem. C* 116 (2012) 26262–26274.
- [26] C. Hammond, M.M. Forde, M.H.A. Rahim, A. Thetford, Q. He, R.L. Jenkins, N. Dimitratos, J.A. Lopez-Sanchez, N.F. Dummer, D.M. Murphy, A.F. Carley, S.H. Taylor, D.J. Willock, E.E. Stangland, J. Kang, H. Hagen, C.J. Kiely, G.J. Hutchings, *Angew. Chem. Int. Ed.* 51 (2012) 5129–5133.
- [27] G.D. Lei, B.J. Adelman, J. Sárkány, W.M.H. Sachther, *Appl. Catal. B* 5 (1995) 245–256.
- [28] Z.R. Ismagilov, S.A. Yashnik, V.F. Anufrienko, T.V. Larina, N.T. Vasenin, N.N. Bulgakov, S.V. Voxel, L.T. Tsykoza, *Appl. Surf. Sci.* 226 (2004) 88–93.
- [29] H.H. Tjippins, *Phys. Rev. B* 1 (1970) 126–135.
- [30] L. Lu, L.P. Li, X.J. Wang, G.S. Li, *J. Phys. Chem. B* 109 (2005) 17151–17156.
- [31] M. Iwamoto, H. Yahiro, K. Tanda, N. Mizuno, Y. Mine, S. Kagawa, *J. Phys. Chem.* 95 (1991) 3727–3730.
- [32] S.A. Yashnik, V.F. Anufrienko, V.A. Sazonov, Z.R. Ismagilov, V.N. Parmon, *Kinet. Catal.* 53 (2012) 363–373.
- [33] M.H. Groothaert, J.A. van Bokhoven, A.A. Battiston, B.M. Weckhuysen, R.A. Schoonheydt, *J. Am. Chem. Soc.* 125 (2003) 7629–7640.

- [34] G. Moretti, C. Dossi, A. Fusi, S. Recchia, R. Psaro, *Appl. Catal. B* 20 (1999) 67–73.
- [35] M.S. Kumar, M. Schwidder, W. Grünert, U. Bentrup, A. Brückner, *J. Catal.* 239 (2006) 173–186.
- [36] C. Li, *J. Catal.* 216 (2003) 203–212.
- [37] K.Q. Sun, H.A. Xia, Z.C. Feng, R. van Santen, E. Hensen, C. Li, *J. Catal.* 254 (2008) 383–396.
- [38] K.J. Sun, F.T. Fang, H.A. Xia, Z.C. Feng, W.X. Li, C. Li, *J. Phys. Chem. C* 112 (2008) 16036–16041.
- [39] R.Q. Long, R.T. Yang, *J. Catal.* 198 (2001) 20–28.
- [40] N. Katada, H. Igi, J.-H. Kim, M. Niwa, *J. Phys. Chem. B* 101 (1997) 5969–5977.
- [41] G.H. Kuehl, H.K.C. Timken, *Microporous Mesoporous Mater.* 35–36 (2000) 521–532.
- [42] S. Brandenberger, O. Kröcher, A. Wokaun, A. Tissler, R. Althoff, *J. Catal.* 268 (2009) 297–306.
- [43] H. Praliud, S. Mikhailenko, Z. Chajar, M. Primet, *Appl. Catal. B* 16 (1998) 359–374.
- [44] T. Nanba, S. Masukawa, A. Ogata, J. Uchiawa, A. Obuchi, *Appl. Catal. B* 61 (2005) 288–296.
- [45] M. Richter, M.J.G. Fait, R. Eckelt, M. Schneider, J. Radnik, D. Heidemann, R. Fricke, *J. Catal.* 245 (2007) 11–24.
- [46] M.H. Kim, I.-S. Nam, Y.G. Kim, *J. Catal.* 179 (1998) 350–360.
- [47] D. Chadwick, T. Hashemi, *Corros. Sci.* 18 (1978) 39–51.
- [48] J.L. Gong, H.R. Yue, Y.J. Zhao, S. Zhao, L. Zhao, J. Lv, S.P. Wang, X.B. Ma, *J. Am. Chem. Soc.* 134 (2012) 13922–13925.
- [49] S.J. Roosendaal, B. van Asselen, J.W. Elsenaar, A.M. Vredenberg, F.H.P.M. Habraken, *Surf. Sci.* 442 (1999) 329–337.
- [50] C.L. Bracey, P.R. Ellis, G.J. Hutchings, *Chem. Soc. Rev.* 38 (2009) 2231–2243.
- [51] M.C. Che, Z.X. Cheng, C. Louis, *J. Am. Chem. Soc.* 117 (1995) 2008–2018.
- [52] Y.I. Yermakov, B.N. Kuznetsov, I.A. Ovsyannikova, A.N. Startsev, S.B. Erenburg, M.A. Sheromov, *React. Kinet. Catal. Lett.* 8 (1978) 377–382.
- [53] T. Cheng, Z.Y. Fang, Q.X. Hu, K.D. Han, X.Z. Yang, Y.J. Zhang, *Catal. Commun.* 8 (2007) 1167–1171.
- [54] E. Boellaard, F.T. van de Scheur, A.M. van der Kraan, J.W. Geus, *Appl. Catal. A* 171 (1998) 333–350.
- [55] L.Z. Zhang, X.Q. Wang, J.M. Millet, P.H. Matter, U.S. Ozkan, *Appl. Catal. A* 351 (2008) 1–8.
- [56] A. Trovarelli, *Comments Inorg. Chem.* 20 (1999) 263–284.
- [57] J. Ereña, R. Garoña, J.M. Arandes, A.T. Aguayo, J. Bilbao, *Catal. Today* 107–108 (2005) 467–473.
- [58] A. Sultana, T. Nanba, M. Sasaki, M. Haneda, K. Suzuki, H. Hamada, *Catal. Today* 164 (2011) 495–499.